Progress in Reaction Kinetics and Mechanism

ARTICLE

Open Access

https://doi.org/10.48130/prkm-0026-0002

Progress in Reaction Kinetics and Mechanism **2026**, 51: e011

Experimental study of the co-pyrolysis of bamboo and waste tires by TG-FTIR-GC/MS

Yang Bai[1], Na Du[2*], Zhipeng Zhou[1] and Hongting Ma[1]

[1] *Tianjin Key Laboratory of Built Environment and Energy Application, Tianjin University, Tianjin 300072, China*

[2] *Heibei Province Low-carbon and Clean Building Heating Technology Innovation Center, School of Civil Engineering and Mechanics, Yanshan University, Qinhuangdao 066004, China*

* Correspondence: nadu@ysu.edu.cn (Du N)

Abstract

The co-pyrolysis of bamboo (BB) and waste tires (WT) is a promising waste-to-energy strategy; however, a fundamental understanding of its reaction kinetics and real-time volatile interactions remains limited. This study addresses this gap by employing an integrated TG-FTIR-GC/MS approach to elucidate the synergistic mechanisms, kinetics, and product evolution of BB/WT co-pyrolysis. Marked synergy was observed between 300–500 °C for blends of 5:5, and 3:7 (BB : WT). At the 5:5 ratio, the phenolic, ketone, and alkene contents decreased to 12.42%, 13.37%, and 51.91%, respectively. At the 3:7 ratio, the phenolic and ketone contents further decreased to 2.65% and 5.96%, respectively, with alkenes accounting for 61.18%. The activation energies for BB, WT, and their 1:1 blend, determined using the KAS, FWO, and Friedman methods, were 101.91, 117.04, and 113.67 kJ/mol, respectively. The Coats-Redfern method identified A2/3 for BB, F3/2 for WT, and D3 for the 1:1 blend as the most suitable reaction models. These findings provide crucial insights for optimizing the co-pyrolysis process, and enhancing the efficient utilization of biomass and WT.

Citation: Bai Y, Du N, Zhou Z, Ma H. 2026. Experimental study of the co-pyrolysis of bamboo and waste tires by TG-FTIR-GC/MS. *Progress in Reaction Kinetics and Mechanism* 51: e011 https://doi.org/10.48130/prkm-0026-0002

Introduction

Biomass is particularly attractive because of its renewability, wide availability, and potential carbon neutrality[1,2]. Among the various biomass resources, bamboo (BB) is particularly attractive because of its fast growth rate, high carbon sequestration capacity, wide distribution in tropical and subtropical regions, and non-competition with agricultural land[3,4]. These features not only highlight its renewability, but also reinforce its role in climate change mitigation and carbon-neutral strategies. In China, BB resources exceed 6.67 million ha, generating an annual economic value of nearly 320 billion yuan, highlighting its strategic importance as a sustainable feedstock for energy production[5].

Pyrolysis, a thermal decomposition process in an oxygen-free environment, is a promising method for converting biomass into valuable products[6]. It not only reduces waste and mitigates disposal issues, but also generates bio-oil, biochar, and syngas, thus providing marked techno-economic viability[7]. Despite these advantages, biomass pyrolysis faces inherent challenges. Bio-oil usually contains a high proportion of oxygenated compounds, exhibits high water content, low calorific value, high viscosity, and strong acidity, all of which limit its direct utilization as fuel[8,9]. Although BB is an abundant and rapidly renewable biomass, it shares these limitations when subjected to pyrolysis alone, which constrains its potential as a standalone energy feedstock[10].

Waste tires (WT) have gained attention as a potential feedstock for energy recovery, with a global generation of over 17 million tons in 2020, and a projection of 120 million tons by 2030[11]. Their high carbon content and rubber-based composition make them valuable sources of carbon-based energy[12]. However, improper disposal of WT, such as landfilling and open burning, poses severe environmental risks, including soil contamination, fire hazards, and toxic emissions[13,14]. Pyrolysis has been extensively studied as an environmentally sustainable route for WT recycling, generating value-added products such as carbon black, activated carbon, liquid fuels, and syngas[15,16], while simultaneously promoting waste reduction and pollution control[17,18]. However, WT has a relatively uniform composition, which limits the variety and upgrading potential of pyrolysis products[19,20].

According to the definition of the effective hydrogen-to-carbon ratio (H/C_{eff})[21], biomass is generally characterized by low H/C_{eff} values (0–0.3), which are associated with the poor quality of its derived bio-oil[22]. In contrast, WT exhibits a much higher H/C_{eff}[23], and its co-pyrolysis with biomass has been recognized as an effective strategy to exploit synergistic effects, and improve both the product yield and quality[23,24]. For instance, Kumar et al.[25] reported that the co-pyrolysis of de-oiled microalgal residue with WT significantly modified the chemical composition of bio-oil, and increased its yield to 48.96% wt, indicating improvements in both bio-oil and biochar quality. Similarly, Farooq et al.[26] demonstrated that incorporating WT into wheat straw pyrolysis enhanced the calorific value of bio-oil, while reducing its oxygenated compound content. Notably, Niu et al.[19] compared the co-pyrolysis of WT with rice husks, wheat straw, and BB, and found that although synergistic effects were observed in all cases, the wheat straw-BB blends exhibited particularly strong synergy. This highlights the potential of BB as a promising feedstock for co-pyrolysis with WT.

Several studies have investigated the co-pyrolysis of BB and WT, focusing on their product characteristics and synergistic interactions. Guo et al.[27] analyzed the release characteristics of oxygen-containing compounds and aromatics during the co-pyrolysis of WT and BB by pyrolysis gas-chromatography/mass spectrometry(Py-GC/MS). The active oxygen-containing free radicals released from BB sawdust promoted the chain breaking of rubber components and the release of hydrogen-free radicals. Niu et al.[19] demonstrated that BB facilitated the pore structure development of biomass char,

suppressed aromatic hydrocarbon formation, and promoted the production of alicyclic hydrocarbons, ethers, and furan. Wang et al.[22,28] conducted catalytic fast co-pyrolysis of BB and WT over CaO/HZSM-5 and MgO/HZSM-5. The results indicated that the dual catalysts effectively enhanced the bio-oil quality by promoting the formation of aromatics and olefins while suppressing undesirable oxygenates. Wang et al.[29] investigated microwave-assisted catalytic fast co-pyrolysis of BB and WT using HZSM-5, and reported that the process maximized bio-oil yield at 550 °C, while enhancing aromatic hydrocarbon production through the hydrogen-donating effect of WT. Regarding the solid residue, Deng et al.[30] highlighted the microstructural evolution during co-pyrolysis. It was observed that the process achieves an organic integration of the fibrous BB framework with the WT-derived carbon matrix. The diffusion of tire-derived radicals into biomass-derived pores facilitates crosslinking reactions, which effectively mitigates agglomeration, and enhances pore connectivity compared to the individual materials.

Although the co-pyrolysis of BB and WT has been investigated, the reported synergistic effects mainly focus on improvements in pyrolysis products, such as enhanced oil yield, modified composition, and catalytic upgrading of bio-oil. However, the fundamental understanding of the reaction kinetics, which is critical for reactor design, and the *in situ* volatile interaction mechanisms driving these synergies remain inadequately explored. For instance, although recent work has advanced the understanding of co-pyrolysis synergies[31], a comprehensive kinetic analysis coupled with real-time volatile product evolution for the BB-WT system is still lacking. Consequently, the fundamental understanding of BB-WT interactions remains limited, and the lack of reliable kinetic data continues to hinder process optimization and the potential scale-up of BB-WT co-pyrolysis.

To address these research gaps, this study characterizes the co-pyrolysis behavior and reaction kinetics of BB-WT blends, by integrating thermogravimetric analysis, fourier transform infrared spectroscopy, and gas chromatography-mass spectrometry (TG-FTIR-GC/MS). The key novelties and contributions are as follows:

(1) The co-pyrolysis behaviors of BB, WT, and their blends were studied using a TG-FTIR-GC/MS approach, which enabled the simultaneous evaluation of the thermal degradation behaviors, weight-loss patterns, and gaseous product evolution, offering a more holistic understanding of BB-WT interactions.

(2) The pyrolysis kinetics of the BB-WT blends were determined using the KAS, FWO, Friedman, and Coats-Redfern methods, establishing reliable reaction models and activation energies. These models provide critical parameters for understanding blend interactions and offer a theoretical basis for optimizing and scaling-up co-pyrolysis processes.

(3) By linking the thermal degradation behavior, chemical composition of volatile products, and kinetic parameters, this study provides a holistic view of the co-pyrolysis process, which can facilitate the optimization of the process for energy recovery and chemical production.

The findings not only fill a critical knowledge gap in BB-WT co-pyrolysis, but also establish a solid theoretical basis that can guide process optimization, improve energy recovery efficiency, and support future industrial applications of waste-to-energy technologies.

Materials and methods

Materials

The BB samples used in this study were obtained from a chopstick manufacturing facility in Hunan Province, China. The samples were ground using a grinder and sieved through a 150 μm standard mesh to achieve a narrow particle size distribution. In the TG experiments, particles exceeding 0.25 mm in diameter were constrained during heating because of their lower thermal conductivity[32]. Consequently, the material must be ground into a powder with a particle size below 0.2 mm to ensure a more stable heat transfer rate[33]. WT particles were provided by Hunan Qiheng Environmental Protection Technology Co., Ltd, and were processed through a two-stage crushing line to remove steel wires before use. Owing to the small sample mass in the TG experiments and the differing densities of the biomass and polymer, each component was individually weighed using an analytical microbalance, and thoroughly blended using a mortar and pestle. The homogeneity of the BB-WT blends was verified through three repeated TG runs, which produced nearly overlapping TG/DTG curves (Supplementary Fig. S1), with a relative standard deviation (RSD) of key thermal parameters (e.g., peak temperature and mass loss at characteristic points) within 0.5%.

Proximate analysis of the samples was conducted following the Chinese standards GB/T 212-2008[34] and CJ/T 313-2009[35]. The elemental compositions of C, H, O, N, and S were determined using an elemental analyzer (5E-CHN2200) in accordance with CJ/T 96-2013[36]. Additionally, the higher heating value (HHV) of the feedstock was measured using an automatic calorimetric bomb (5E-AC). The results are presented in Table 1.

TG and TG-FTIR-GC/MS experiments

Thermogravimetric (TG) analyses were performed using an STA-8000 instrument (PerkinElmer, USA) under a constant flow of high-purity nitrogen gas (99.999%) at 20 mL/min. Approximately 17 mg of the sample was uniformly loaded into ceramic crucibles to minimize heat and mass transfer limitations. Two sets of TG experiments were designed following a controlled-variable approach: (i) to study the effect of the final pyrolysis temperature, the samples (BB, WT, and their 1:1 blend) were heated to 500, 600, 700, 800, and 900 °C, at a heating rate of 20 °C/min; (ii) to study the effect of the heating rate, the samples were heated from room temperature to 700 °C at rates of 10, 20, 30, and 40 °C/min. These TG experiments provided fundamental thermal degradation characteristics and were used to determine the appropriate heating conditions for subsequent coupled analysis.

Based on the TG results, TG-FTIR-GC/MS analyses were performed to investigate the co-pyrolysis behavior and volatile products of the

Table 1. Proximate and ultimate analyses of the samples.

Samples	Proximate analysis (%)					Ultimate analysis (%)				
	M_{ad}	V_{ad}	A_{ad}	FC_{ad}	HHV (MJ/kg)	C	H	O	N	S
BB	12.76	72.14	0.78	14.32	17.62	44.24	5.21	36.64	0.14	0.23
WT	1.23	61.94	13.04	23.79	36.62	76.08	7.15	1.75	0.53	1.75

M: moisture; V: volatile; A: ash; FC: fixed carbon.

samples. The coupled system consisted of a thermogravimetric analyzer (TGA), FTIR spectrometer (Spectrum 3, PerkinElmer), gas chromatograph (TRACE 1600, Thermo Fisher Scientific), and mass spectrometer (ISQ 7610, Thermo Fisher Scientific), which were connected through heated transfer lines to ensure efficient transport of volatile compounds (Fig. 1). To ensure stable operation and representative results, a constant heating rate of 20 °C/min was selected for the coupled experiment. BB and WT were blended at mass ratios of 0:10, 1:9, 3:7, 5:5, 7:3, 9:1, and 10:0, covering the full range from pure WT to pure BB, including low-percentage, intermediate, and high-percentage mixtures, to capture representative interaction patterns of the mixtures. The evolved gases were continuously monitored using FTIR to track the evolution of the functional groups. At the peak weight-loss temperature, the evolved gases were analyzed using GC/MS to elucidate the influence of the blending ratio on the co-pyrolysis product distribution. All experiments were conducted in triplicate to ensure data robustness and reproducibility.

The TG-FTIR transfer line was maintained at 270 °C to ensure the efficient transfer of volatile products. FTIR spectra were collected in the range of 4,000–600 cm^{-1} with a resolution of 8 cm^{-1}, and each scan lasted 2.7 s without signal averaging. The GC/MS system was operated in an online configuration. A TG-1MS column (30 m × 0.32 mm × 0.25 μm) was used. The GC oven program was set as follows: initial temperature 50 °C held for 5 min, ramped up at 10 °C/min to 250 °C, then held for 5 min. High-purity helium served as the carrier gas at a flow rate of 5 mL/min. The GC injection port was maintained at 270 °C under a constant pressure of 100 kPa. The MS was operated with the ion source temperature set at 280 °C, and a scanning mass-to-charge ratio (m/z) range of 41–400.

Reaction kinetics

The rate of the solid heterogeneous reaction can be expressed as follows:

$$\frac{\mathrm{d}\alpha}{\mathrm{d}t} = k(T)f(\alpha) = A\exp\left(-\frac{E}{\mathrm{R}T}\right)f(\alpha) \tag{1}$$

where, α is the conversion of the sample, t is the reaction time, T is the thermodynamic temperature (K), $f(\alpha)$ represents the differential form of the kinetic model function, and $k(T)$ is the temperature-dependent rate constant.

According to the Arrhenius equation, $k(T)$ is defined as:

$$k(T) = A\exp\left(-\frac{E}{\mathrm{R}T}\right) \tag{2}$$

Fig. 1 Photograph of the TG-FTIR-GC/MS experimental setup.

where, A, E, and R, are the pre-exponential factor (min^{-1}), activation energy (kJ/mol), and gas constant (R = 8.314 J/(mol·K)), respectively.

The conversion α can be calculated using the following equation:

$$\alpha = \frac{m_0 - m_t}{m_0 - m_f} \tag{3}$$

where, m_0, m_t and m_f are the initial, time t, and final masses of the sample, respectively.

Incorporating a constant linear heating rate $\beta = \frac{\mathrm{d}T}{\mathrm{d}t}$, Eq. (1) transforms into:

$$\beta\frac{\mathrm{d}\alpha}{\mathrm{d}T} = A\exp\left(-\frac{E}{\mathrm{R}T}\right)f(\alpha) \tag{4}$$

By integrating this temperature, Eq. (1) can also be expressed as

$$G(\alpha) = \int_0^\alpha \frac{d\alpha}{f(\alpha)} = \frac{A}{\beta}\int_0^T \exp\left(-\frac{E}{\mathrm{R}T}\right)\mathrm{d}T \tag{5}$$

where, $G(\alpha)$ refers to the integral form of the kinetic model function.

Table 2 summarizes the expressions of $f(\alpha)$ and $G(\alpha)$ for common kinetic model functions.

The apparent activation energy at different conversions ($E\alpha$) was calculated using model-free methods, which could accurately estimate kinetic parameters without prior knowledge of reaction models[37], making them highly reliable for multi-step processes. KAS[38,39], FWO[40,41], and Friedman[42] methods are based on dynamic heating rates and are considered the most proficient for estimating kinetic restraints[37,43]. Among them, the KAS and FWO methods are integral methods that rely on approximations to integrate the rate equation, whereas Friedman is a differential method that uses the instantaneous reaction rate directly, granting it high sensitivity to changes in reaction rates and mechanisms at different conversions[44]. These methods are described by the following equations:

$$\ln\left(\frac{\beta}{T^2}\right) = \ln\left(\frac{A_\alpha \mathrm{R}}{E_\alpha G(\alpha)}\right) - \frac{E_\alpha}{\mathrm{R}}\frac{1}{T} \tag{6}$$

$$\log(\beta) = \log\left(\frac{A_\alpha E_\alpha}{\mathrm{R}G(\alpha)}\right) - 2.315 - 0.457\frac{E_\alpha}{\mathrm{R}}\frac{1}{T} \tag{7}$$

$$\ln(\beta\frac{\mathrm{d}\alpha}{\mathrm{d}T}) = \ln[A_\alpha f(\alpha)] - \frac{E_\alpha}{\mathrm{R}}\frac{1}{T} \tag{8}$$

The E_α is determined by the slope of the linear representations of $\ln(\frac{\beta}{T^2})$, $\log(\beta)$, and $\ln(\beta\frac{\mathrm{d}\alpha}{\mathrm{d}t})$ against $\frac{1}{T}$, respectively. When the E/R exceeds 5, the error in the calculated E_α is less than 4%[45]. The CR method was used to identify the reaction mechanism. This is an integral method that incorporates the thermal degradation mechanism into the formulation. An asymptotic series expansion was used to estimate the temperature integrals. The CR method is expressed as follows[46]:

$$\ln\frac{G(\alpha)}{T_\alpha^2} = \ln\left[\frac{A\mathrm{R}}{\beta E_\alpha}\left(1 - \frac{2\mathrm{R}T}{E_\alpha}\right)\right] - \frac{E_\alpha}{\mathrm{R}T} \tag{9}$$

By plotting in $\ln\frac{G(\alpha)}{T_\alpha^2}$ against $\frac{1}{T}$, the slope and intercept can be used to evaluate E_α and A. The best-fit reaction model was selected based on the highest coefficient of determination (R^2) value.

When E_α and reaction model $f(\alpha)$ or $g(\alpha)$ are determined, the pre-exponential factor (A_α) can also be estimated using Eqs (6), (7), and (8). The kinetic compensation effect (KCE) can be analyzed through the linear regression of A_α and E_α, by Eq. (10):

$$\ln A_\alpha = \mathrm{a}E_\alpha + \mathrm{b} \tag{10}$$

where, a and b are constants.

Table 2. Common kinetic model functions.

Reaction mechanism model	No.	Code	$G(\alpha)$	$f(\alpha)$	Reaction model
Chemical reaction	1	F1	$-\ln(1-\alpha)$	$1-\alpha$	n = 1 reaction
	2	F3/2	$2[(1-\alpha)^{-1/2}-1]$	$(1-\alpha)^{3/2}$	n = 1.5 reaction
	3	F2	$(1-\alpha)^{-1}-1$	$(1-\alpha)^{2}$	n = 2 reaction
	4	F3	$1/2[(1-\alpha)^{-2}-1]$	$(1-\alpha)^{3}$	n = 3 reaction
Diffusion controlled reaction	5	D1	α^2	$1/2\alpha^{-1}$	Parabolic law
	6	D2	$(1-\alpha)\ln(1-\alpha)+\alpha$	$[-\ln(1-\alpha)]^{-1}$	Valensi equation
	7	D3	$[1-(1-\alpha)^{1/3}]^2$	$3/2(1-\alpha)^{2/3}[1-(1-\alpha)^{1/3}]^{-1}$	Jander equation
	8	G-B	$(1-2/3\alpha)-(1-\alpha)^{2/3}$	$3/2\left[(1-\alpha)^{1/3}-1\right]^{-1}$	Ginstling-Broushtein equation
	9	ZH	$[(1-\alpha)^{-1/3}-1]^2$	$3/2(1-\alpha)^{4/3}[(1-\alpha)^{-1/3}-1]^{-1}$	Zhuralev-Lesokin-Tempelman equation
Phase boundary reaction	10	R1	α	1	1D
	11	R2	$1-(1-\alpha)^{1/2}$	$2(1-\alpha)^{1/2}$	2D, shrinking cylinder
	12	R3	$1-(1-\alpha)^{1/3}$	$3(1-\alpha)^{2/3}$	3D, shrinking sphere
Random nucleation and subsequent	13	A3/2	$[-\ln(1-\alpha)]^{2/3}$	$3/2(1-\alpha)[-\ln(1-\alpha)]^{1/3}$	Aeveami-Erofeev equation
	14	A2	$[-\ln(1-\alpha)]^{1/2}$	$2(1-\alpha)[-\ln(1-\alpha)]^{1/2}$	Aeveami-Erofeev equation
	15	A3	$[-\ln(1-\alpha)]^{1/3}$	$3(1-\alpha)[-\ln(1-\alpha)]^{2/3}$	Aeveami-Erofeev equation
	16	A4	$[-\ln(1-\alpha)]^{1/4}$	$4(1-\alpha)[-\ln(1-\alpha)]^{3/4}$	Aeveami-Erofeev equation
	17	A1	$[-\ln(1-\alpha)]$	$(1-\alpha)$	Aeveami-Erofeev equation
	18	A2/3	$[-\ln(1-\alpha)]^{3/2}$	$2/3(1-\alpha)[-\ln(1-\alpha)]^{-1/2}$	Aeveami-Erofeev equation
	19	A1/2	$[-\ln(1-\alpha)]^{2}$	$1/2(1-\alpha)[-\ln(1-\alpha)]^{-1}$	Aeveami-Erofeev equation
	20	A1/3	$[-\ln(1-\alpha)]^{3}$	$1/3(1-\alpha)[-\ln(1-\alpha)]^{-2}$	Aeveami-Erofeev equation
	21	A1/4	$[-\ln(1-\alpha)]^{4}$	$1/4(1-\alpha)[-\ln(1-\alpha)]^{-3}$	Aeveami-Erofeev equation
Mampel power law	22	P1	$\alpha^{1/4}$	$4\alpha^{3/4}$	Power law
	23	P2	$\alpha^{1/3}$	$3\alpha^{2/3}$	Power law
	24	P3	$\alpha^{1/2}$	$2\alpha^{1/2}$	Power law

Interactions between materials

To evaluate the potential interactions during the co-pyrolysis of the BB-WT blend, the difference in weight loss (ΔW) can be determined as follows[47]:

$$\Delta W = W_{\text{blend}} - (x_{\text{BB}} W_{\text{BB}} + x_{\text{WT}} W_{\text{WT}}) \quad (11)$$

where, W_{blend} represents the experimental weight loss of the blend, and x_{BB} and x_{WT} denote the mass fractions of BB and WT in the blend, respectively. W_{BB} and W_{WT} are the weight losses of the individual components under the same conditions.

Similarly, the difference in weight loss rate (Δr) between the experimental value of the blend and the weighted sum of the individual components is calculated using the following equation:

$$\Delta r = r_{\text{blend}} - (x_{\text{BB}} r_{\text{BB}} + x_{\text{WT}} r_{\text{WT}}) \quad (12)$$

where, Δr is the weight loss rate difference, and r_{BB} and r_{WT} are the weight loss rates of BB and WT, respectively. For both ΔW and Δr, positive values indicated a synergistic effect, whereas negative values indicated an inhibitory effect.

The interactions during the co-pyrolysis of BB and WT were evaluated by examining the activation energies through kinetic analysis. The theoretical E for the blend is given by[47]:

$$E_{\text{Calc}} = x_{\text{BB}} E_{\text{BB}} + x_{\text{WT}} E_{\text{WT}} \quad (13)$$

where, E_{Calc} represents the calculated E of the blend, and E_{BB} and E_{WT} are the experimental activation energies for BB and WT, respectively.

Comparing the E_{Calc} with the experimental E (E_{Exp}) reveals potential interactions. A lower E_{Exp} compared to the E_{Calc} indicates a synergistic effect, suggesting that the blend reacts more easily than expected. Conversely, a higher E_{Exp} suggests an inhibitory effect.

Results and discussion

TG and DTG analysis

Effects of final pyrolysis temperature on TG characteristics

The TG and DTG curves of BB, WT, and their 1:1 blend at final pyrolysis temperatures (T_{final}) of 500, 600, 700, 800, and 900 °C are shown in Fig. 2. The key parameters extracted from the TG and DTG curves are listed in Supplementary Table S1. For BB, major weight loss occurred within 250–450 °C range, reflecting its highly volatile matter and oxygen content, which promoted early devolatilization and rapid degradation. In contrast, the WT displayed more pronounced weight loss in the 400–500 °C range, consistent with its lower volatile matter, higher fixed carbon, and greater elemental carbon content, which together confer higher thermal stability. The blend of BB and WT exhibited intermediate behavior, with the primary devolatilization occurring between 270–520 °C, indicating a combined degradation process. Moreover, the residual yields decreased with increasing T_{final}, from 24.7% to 18.3% for BB, 41.3% to 36.0% for WT, and 32.2% to 27.1% for the blend, respectively. At 700 °C, the residual mass of all feedstocks was sufficiently low, indicating near complete pyrolysis; thus, 700 °C was selected as the final pyrolysis temperature for subsequent analyses.

The DTG curves provide further insights into the decomposition characteristics. For BB, two distinct peaks were observed: a minor peak at approximately 98 °C (T_{p1}), attributed to moisture volatilization, and a major peak at approximately 384 °C (the temperature for the maximum weight-loss rate, T_{p2}), corresponding to the main decomposition of organic materials. For WT, only a single dominant peak was detected at approximately 418 °C, indicating that the main degradation occurred at a slightly higher

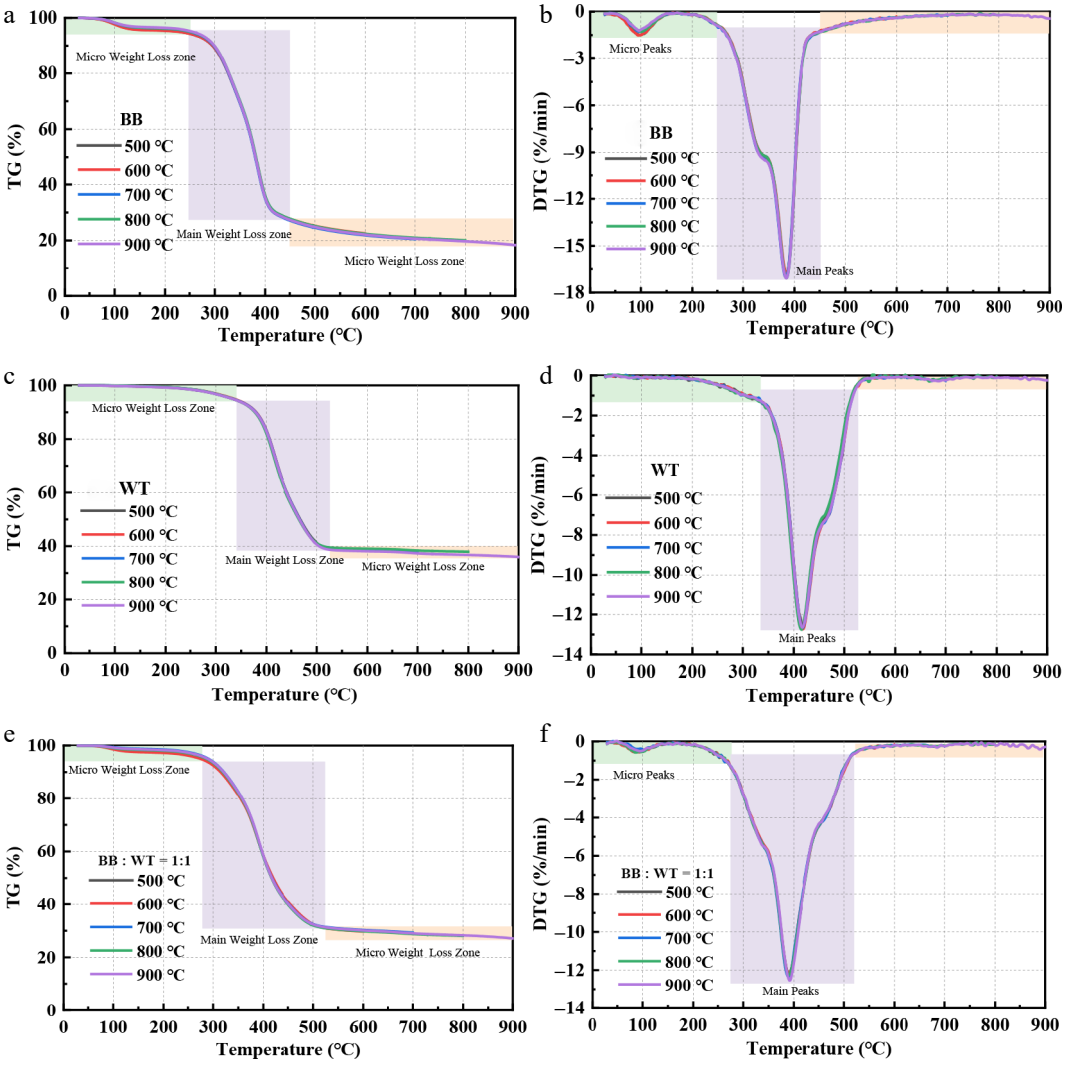

Fig. 2 TG and DTG curves of BB, WT, and their blends at different T_{final}.

temperature range than that of BB. In contrast, the blend exhibited dual peaks, with a micro peak at approximately 94 °C, and a primary peak at approximately 390 °C, reflecting the combined effects of both components. The maximum weight-loss rates (MWLRs) for BB, WT, and the blend showed only minor variations with increasing T_{final}, indicating a consistent degradation behavior.

Effects of heating rates on TG characteristics

Figure 3 illustrates the TG and DTG curves for BB, WT, and their 1:1 blend at heating rates of 10, 20, 30, and 40 °C/min. As the heating rate increased, both the TG and DTG curves shifted towards higher temperature regions, accompanied by an increase in the MWLR's. For BB, the T_{p2} increased from 362.5 °C at 10 °C/min to 409.67 °C at 40 °C/min (a shift of ~47 °C), whereas the MWLR increased from 8.66%/min to 32.86%/min. WT shows a slightly larger T_{p2} shift, from 392.7 °C to 445.8 °C (~53 °C), with the MWLR increasing from 6.02%/min to 24.94%/min. The blend exhibited intermediate T_{final} behavior, with T_{p2} shifting from 366.8 to 415.7 °C, and the MWLR increasing from 5.81% to 23.49%/min. Overall, higher heating rates delayed but intensified the decomposition across all samples, as reflected by the higher peak temperatures and increased weight loss rates. This behavior arises because faster heating reduces the time available for heat conduction within the sample and for volatile products to diffuse outward, thereby lowering the effective heat-transfer efficiency. Consequently, the interior of the particles experiences a thermal lag, requiring higher external temperatures to reach the same decomposition level. Once this threshold was exceeded, the accumulated energy release and volatile liberation occurred more abruptly, producing sharper DTG peaks and higher MWLR's.

Effects of blending ratios on TG characteristics

Figure 4 shows the TG and DTG curves of the BB-WT blends at different blending ratios. These curves are crucial for understanding the influence of the blending ratio on the thermal degradation behavior of the samples. The key TG and DTG parameters are listed in Supplementary Table S1. The TG curves in Fig. 4a show that the thermal degradation profiles of the BB-WT blends varied significantly with different blending ratios. As the proportion of WT increased, the TG curves shifted towards higher temperatures, and the overall weight loss decreased gradually from 79.5% to 70.73%, reflecting the combined thermal behaviors of BB and WT. The DTG curves in Fig. 4b show that with increasing WT content, the DTG curves also shift towards higher temperatures, but the T_{p2} remains largely unchanged, whereas the MWLR decreases. These findings suggest possible interactions between BB and WT during co-pyrolysis.

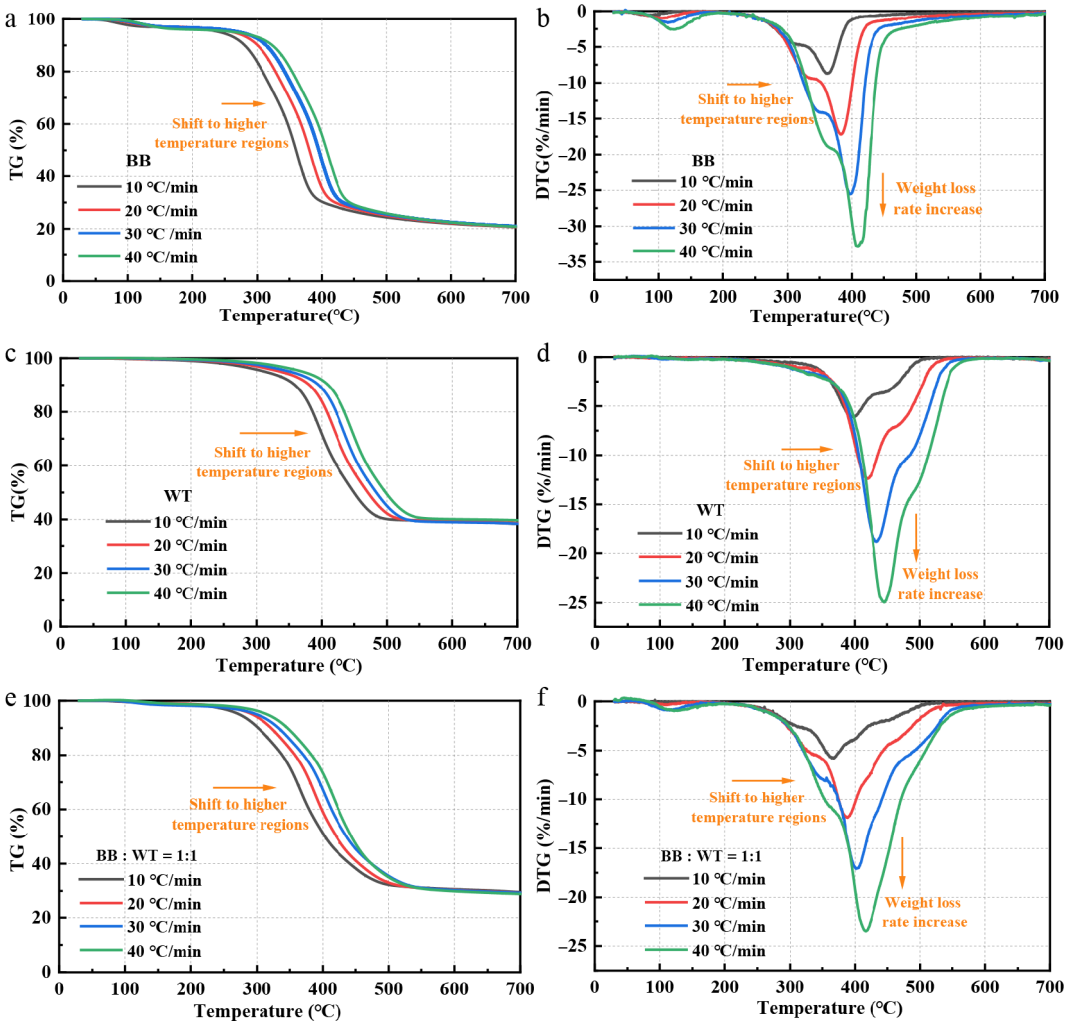

Fig. 3 TG and DTG curves of BB, WT, and their blends at different heating rates.

The interactions of co-pyrolysis

ΔW and Δr were employed to assess the potential synergistic or inhibitory effects during BB-WT co-pyrolysis. As shown in Fig. 5, the ΔW curves indicate the deviation of the actual weight loss from the predicted weight loss based on the individual components. At lower temperatures (below 300 °C), the ΔW values were negative and relatively stable for all blends, indicating negligible interactions in this temperature range. However, between 300 and 500 °C, ΔW fluctuated between negative and positive values, indicating pronounced synergistic effects[47]. The first peak reached its minimum at approximately 350 °C, whereas the second peak was generally positive, with the largest ΔW variations observed for the 3:7 and 5:5 blends, suggesting the highest degree of synergy. Above 500 °C, the ΔW values stabilized, implying that the interactions played a minor role at these higher temperatures. Similarly, the Δr values provide complementary insights. At temperatures below 300 °C, the Δr values remained close to zero, suggesting minimal interaction. With increasing temperature, the Δr values became more pronounced, fluctuating between negative and positive in the 300–500 °C range. Marked positive Δr peaks were observed for the 3:7 and 5:5 blends, reinforcing the synergistic effect inferred from the ΔW analysis. The synergy is attributed to radical interactions where hydrogen donors from WT quench BB-derived oxygenated radicals (e.g., phenoxy radicals)[48], facilitating the observed deoxygenation (reduced phenols/ketones) and enhanced olefin formation (TG-GC/MS analysis of evolved volatiles during co-pyrolysis).

The variations in ΔW and Δr between 300 and 500 °C can be attributed to several factors. First, the release and subsequent interactions of volatile compounds from BB and WT likely accelerated the overall degradation process, as reflected by negative ΔW and positive Δr values. This indicates that more volatile products were generated and decomposed than expected, highlighting the synergistic effects between the components. Second, the coexistence of BB and WT alters pyrolysis reaction pathways, further contributing to synergistic effects. Finally, the stability of the char structure plays a crucial role. At higher temperatures (above 400 °C), positive ΔW and negative Δr values suggest the formation of a more stable char. This stabilization can be linked to amorphous carbon deposition and hydrodeoxygenation reactions, which reduce the porosity and reactivity of the char[49]. Consequently, the char yield increased, whereas the degradation rate was suppressed, leading to an inhibitory effect. Collectively, these factors demonstrate the complex interplay between BB and WT during co-pyrolysis, where both synergistic and inhibitory effects emerge, depending on temperature.

TG-FTIR analysis of evolved volatiles during co-pyrolysis

Supplementary Fig. S2 presents the 3D FTIR spectra of gaseous products evolved during the co-pyrolysis of BB and WT at various

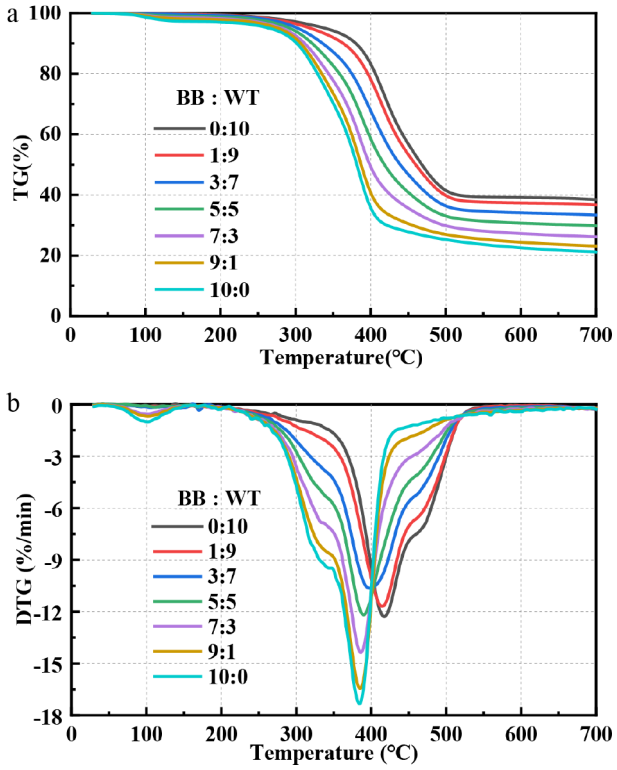

Fig. 4 TG and DTG curves of BB-WT blends at different blending ratios.

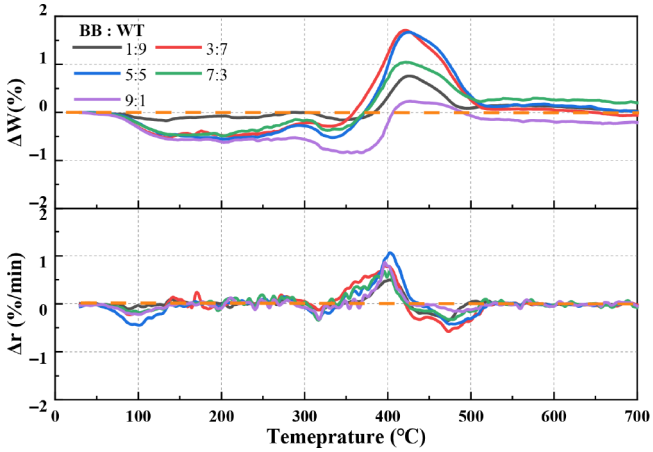

Fig. 5 Interactions during the co-pyrolysis of BB-WT blends.

blending ratios. The main absorption bands include -CH_3 stretching/bending (2,932 and 1,456 cm^{-1}), =C-H wagging (892 cm^{-1}), aromatic ring vibration, and C-H out-of-plane bending (1,508 and 668 cm^{-1}), carbonyl groups (1,750–1,796 cm^{-1}), and CO_2 (2,324/2,360 cm^{-1}), as shown in Table 3. Figure 6 shows the FTIR spectra of the volatile products released during the co-pyrolysis of BB and WT at different blending ratios. Hydrocarbon peaks (2,932 and 1,456 cm^{-1}) were most intense in pure WT, but became weaker as the BB content increased; nevertheless, their onset shifted to lower temperatures and broadened at BB : WT = 3:7 and 5:5, indicating that oxygenated radicals from BB facilitated the earlier scission of WT chains. The olefinic band (892 cm^{-1}) similarly showed maximum intensity in the WT-rich blends, but was suppressed and shifted under intermediate ratios, suggesting further conversion to aromatics. The aromatic bands exhibited complementary behaviors: the 668 cm^{-1} signal was strongest in BB-rich blends, and weakened

Table 3. Characteristic wavenumber bands of functional groups and evolved gases.

Wavelength (cm^{-1})	Functional group	Species assignment	Ref.
2,932	$-CH_3$, stretching vibration	Hydrocarbons	[50]
2,324/2,360	C=O, stretching vibration	CO_2	[51]
1,796, 1,774, and 1,750	–C=O, stretching vibration	Aldehydes and ketones	[50]
1,508	Aromatic ring vibration	Aromatic	[50]
1,456	$-CH_3$, bending vibration	Hydrocarbons	[50]
892	=C–H, wagging vibration	Alkene	[52]
668	–C–H, out-of-plane bending	Benzene	[53]

with WT addition, while the 1,508 cm^{-1} band remained dominant in BB and extended to higher temperatures. At BB : WT = 3:7 and 5:5, the 1,508 cm^{-1} peak broadened and the 668 cm^{-1} peak shifted, reflecting the accelerated aromatization of BB fragments by hydrogen/alkyl radicals from WT, and partial suppression of condensation at high temperatures.

As shown in Fig. 6, for oxygen-containing volatiles, the carbonyl bands (1,750–1,796 cm^{-1}) were the strongest and most persistent in BB-rich blends, consistent with the release of aldehydes and ketones from polysaccharides and lignin. At BB:WT ratios of 3:7 and 5:5, the carbonyl signals were clearly reduced compared to those in the BB-rich blends and displayed an earlier decline, suggesting that the hydrogen/alkyl radicals from WT facilitated the destabilization and conversion of these oxygenates. Correspondingly, the CO_2 bands (2,324/2,360 cm^{-1}) remained relatively strong at these intermediate ratios and exhibited a slight forward shift, whereas their intensity decreased significantly in the WT-rich blends. These results imply that the presence of WT promoted more efficient deoxygenation of BB intermediates, converting unstable oxygenates into CO_2 and thereby suppressing secondary condensation and char formation. Overall, the co-pyrolysis of BB and WT demonstrated distinct synergistic effects: oxygenated radicals from BB lowered the activation barrier for WT degradation, whereas hydrogen donors from WT enhanced the deoxygenation of BB intermediates. Synergy was most pronounced at BB:WT ratios of 3:7 and 5:5, where earlier and broader hydrocarbon/aromatic release coincided with efficient deoxygenation, outperforming either the BB- or WT-rich extremes.

Figure 7 presents the FTIR spectra of the gaseous products evolved during the co-pyrolysis of BB and WT at T_{p2}. Hydrocarbon bands (-CH_3 stretching at 2,932 cm^{-1} and -CH_3 bending at 1,456 cm^{-1}) were the strongest in WT-rich blends and decreased progressively with increasing BB, indicating less aliphatic fragment release at T_{p2}. The olefinic band at 892 cm^{-1} was likewise the most intense in the WT-rich samples and weakened as BB increased. In contrast, the aromatic bands at 1,508 $cm^{-1}$and 668 cm^{-1} were more pronounced in the BB-rich blends, reflecting lignin-derived aromatics. The carbonyl bands (1,750–1,796 cm^{-1}) were also enhanced with increasing BB content, and the CO_2 signals at 2,324/2,360 cm^{-1} were relatively strong for the BB-rich and intermediate ratios. By integrating the FTIR peak areas of different mixtures at temperature T_{p2}, a semi-quantitative analysis was conducted on the variation in the ratio of carbonyl bands/hydrocarbon bands. For BB:WT ratios of 0:10, 1:9, 3:7, 5:5, 7:3, 9:1, and 10:0, the ratios were 0.012, 0.027, 0.076, 0.227, 0.344, 0.400, and 0.465, respectively. Overall, the spectra at BB:WT = 3:7 and 5:5 displayed coexisting features-appreciable hydrocarbons together with carbonyls and CO_2, indicating concurrent WT chain scission and BB deoxygenation at T_{p2}. This compositional balance is consistent with the synergistic interactions inferred from Fig. 6. Oxygenated radicals from BB assist WT scission, whereas

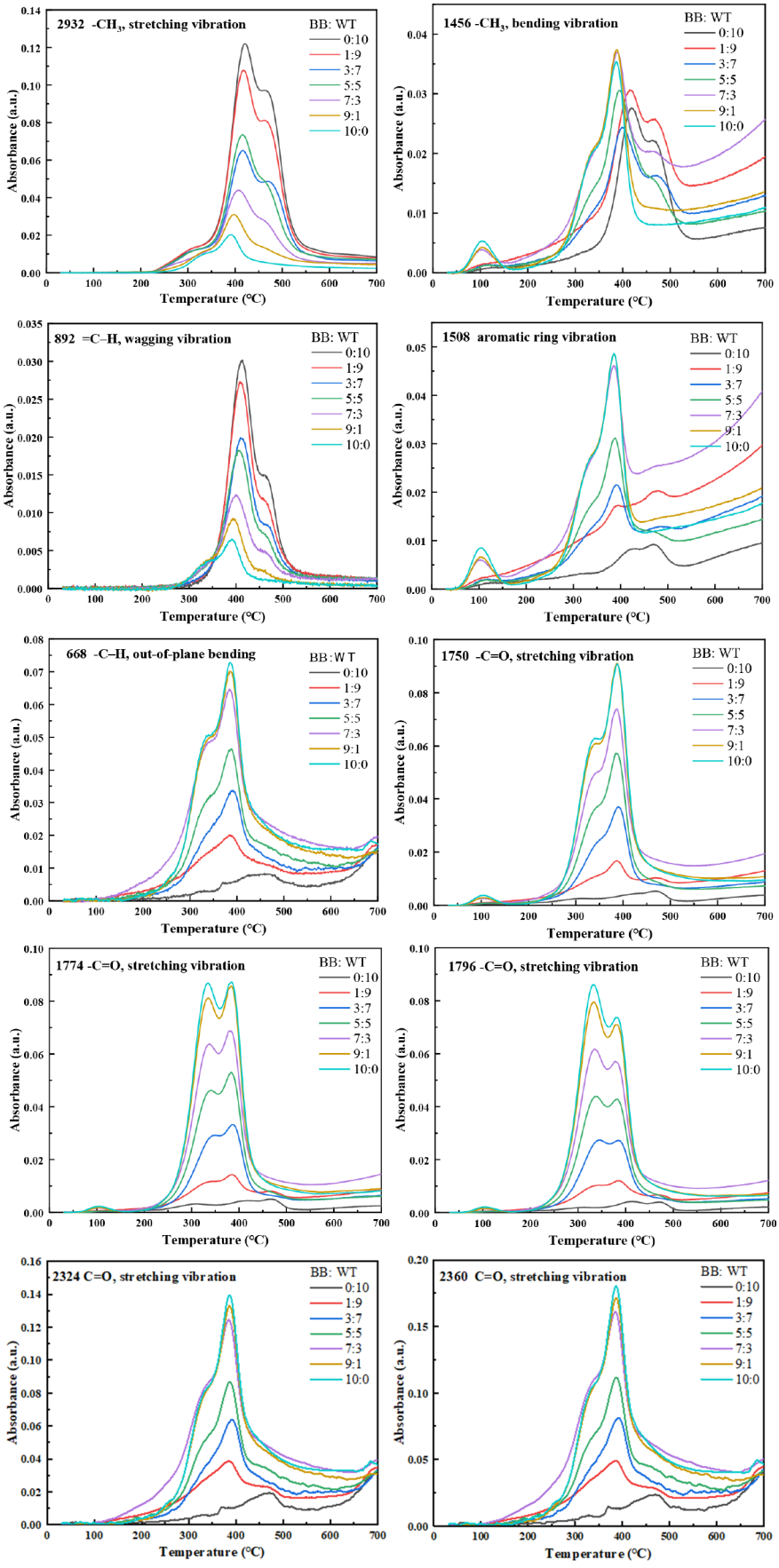

Fig. 6 FTIR evolution of characteristic functional groups with temperature during co-pyrolysis of BB-WT blends.

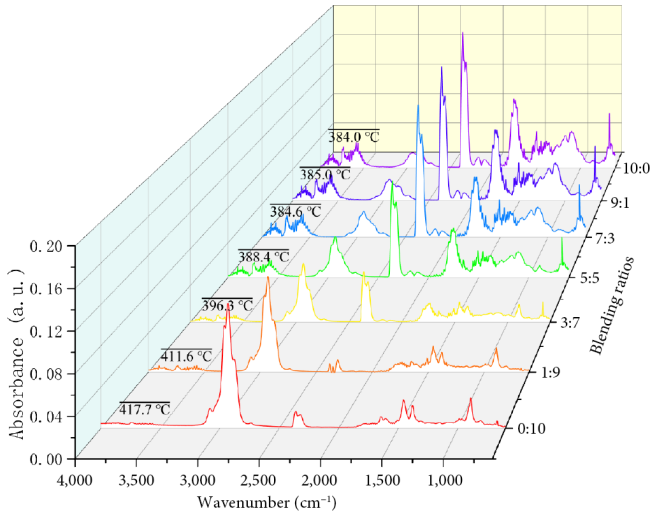

Fig. 7 FTIR spectra of T_{p2} during co-pyrolysis.

WT-derived hydrogen/alkyl radicals facilitate the deoxygenation of BB intermediates.

TG-GC/MS analysis of evolved volatiles during co-pyrolysis

Figure 8 and Supplementary Table S2 show the GC/MS chromatograms of the volatile products at T_{p2} for different BB:WT ratios. Clear compositional differences were observed among the blends. For pure WT, hydrocarbons dominated the spectrum, with styrene contributing 2.07%, and cyclohexene derivatives reaching 31.09%, originating mainly from the decomposition of polystyrene and styrene-butadiene rubber. In contrast, pure BB yielded predominantly oxygenated compounds, including 1,2-cyclopentanedione (11.52%), phenol (16.59%), and 2,6-dimethoxyphenol (9.66%), which reflect the degradation pathways of cellulose and lignin. At intermediate ratios, particularly 3:7 and 5:5, the composition shifted toward a more balanced volatile compound profile. For example, at 5:5, the relative content of 1,4-dimethyl-2-ethylbenzene reached 7.83%, whereas that of 2,6-dimethoxyphenol decreased to 2.63%. Similarly, at 3:7, cyclohexene derivatives remained abundant, whereas phenolic oxygenates were much less prominent than those in BB alone. These observations demonstrate that co-pyrolysis moderates the extremes of each feedstock, reducing the overproduction of phenolics from BB, while maintaining substantial amounts of hydrocarbons from WT.

Figure 9 illustrates the relative distribution of the major product groups at different BB:WT ratios. Pure WT produced mainly hydrocarbons, with alkenes and aromatic hydrocarbons accounting for 63.49% and 14.43%, respectively, together making up nearly 80% of the products, whereas oxygenates were negligible. In contrast, pure BB yielded mostly oxygenated compounds, with phenols reaching 52.37% and ketones 24.72%, with no alkenes detected. With increasing BB fraction, phenols, and ketones became more prominent, whereas hydrocarbons decreased, reflecting the distinct pyrolysis behaviors of biomass and plastics. A clear synergistic effect emerged at intermediate ratios, particularly at 3:7 and 5:5. Compared with pure BB (phenolics 52.37%, ketones 24.72%), both phenolics and ketones were markedly suppressed, whereas hydrocarbons remained substantial. At the 5:5 ratio, phenolics decreased to 12.42%, ketones to 13.37%, and alkenes contributed 51.91%. Similarly, at the 3:7 ratio, phenolics decreased to 2.65% and ketones to

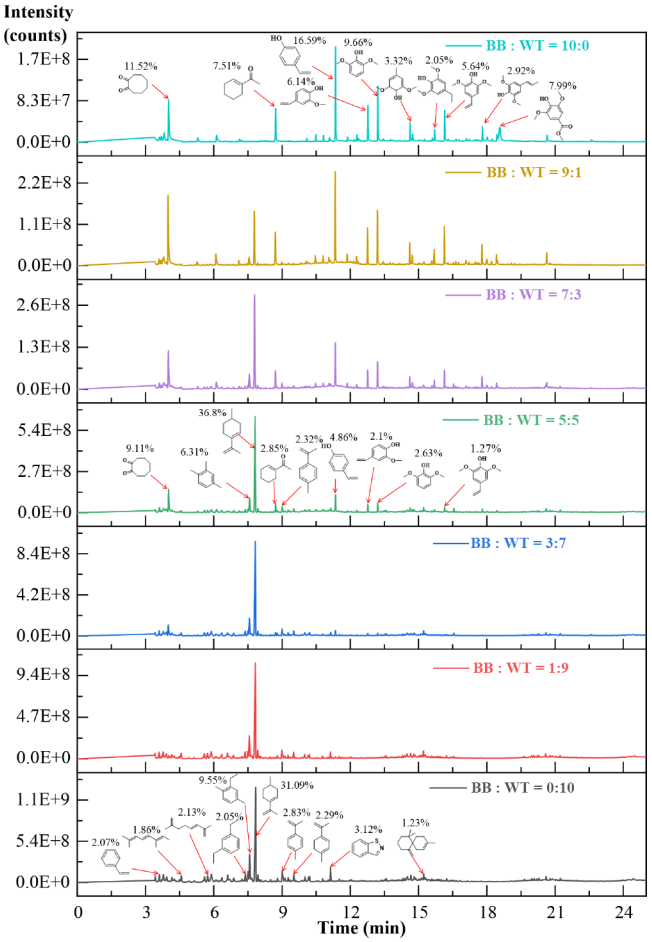

Fig. 8 GC/MS of T_{p2} during co-pyrolysis.

5.96%, whereas alkenes accounted for 61.18%. This balanced distribution can be explained by radical interactions, where hydrogen-rich fragments from WT promote the deoxygenation of BB-derived intermediates, reducing unstable phenolics, whereas oxygen-centered radicals from BB facilitate chain scission in WT, enhancing the release of aromatics and alkenes. The 3:7 and 5:5 blends provided the most favorable outcomes, simultaneously improving fuel quality through lower oxygen content and higher hydrocarbon yield, while retaining moderate oxygenates of chemical value, underscoring the synergistic benefits of BB-WT co-pyrolysis.

Pyrolysis kinetics analysis

Estimation of activation energy

The E_α of BB, WT, and the 1:1 BB-WT blend during pyrolysis was determined by KAS, FWO, and Friedman methods, as shown in Table 4. All methods demonstrated high linearity (Supplementary Fig. S3), with correlation coefficients above 0.95 in the conversion range of 0.1–0.8, indicating the reliability of the calculated E_α values. When the conversion exceeded 0.8, the fitting quality decreased slightly, with the lowest R^2 around 0.87. This reduction is likely associated with the increased complexity of the reaction at higher conversion levels, where additional processes, such as secondary or competing reactions, may reduce the validity of the simplified assumptions underlying these model-free methods[43]. The E_α estimated from KAS, FWO and the Friedman models was altered from 80.0–154.5, 84.9–158.1, and 73.3–186.9 kJ/mol for BB, 75.9–135.4, 82.0–140.7, and 95.7–146.4 kJ/mol for WT, and

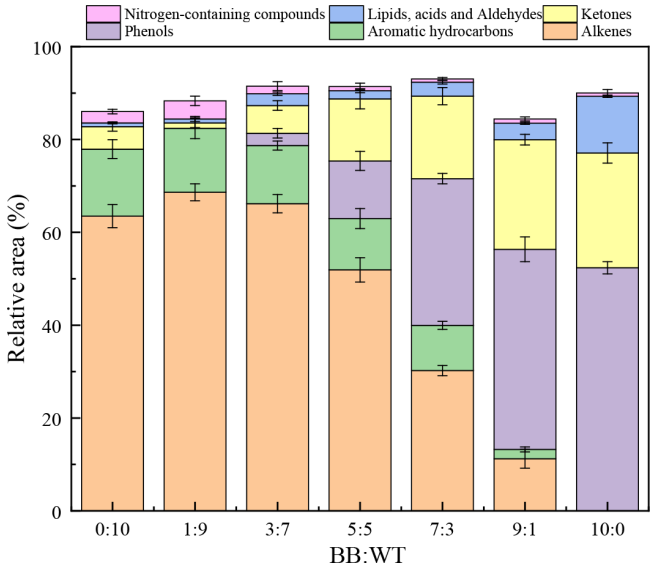

Fig. 9 Relative percentage of chemical compounds in co-pyrolysis of BB and WT.

Table 4. *E* of BB, WT, and their blend at different conversion.

α	BB			WT			BB : WT = 1:1		
	KAS	FWO	Friedman	KAS	FWO	Friedman	KAS	FWO	Friedman
0.1	80.0	84.9	73.3	75.9	82.0	95.7	80.8	85.9	82.2
0.15	78.7	83.9	81.5	88.2	94.2	104.9	83.8	89.1	90.9
0.2	80.8	86.2	87.9	93.6	99.5	108.9	87.9	93.2	98.2
0.25	82.4	87.8	92.1	97.2	103.0	111.3	91.7	97.0	101.3
0.3	84.6	90.1	95.8	99.7	105.5	114.0	94.1	99.5	100.3
0.35	87.6	93.0	98.3	102.0	107.7	116.8	95.3	100.8	100.0
0.4	90.9	96.3	99.6	104.2	109.9	118.8	96.6	102.1	104.8
0.45	91.8	97.2	97.9	106.2	111.9	121.6	98.1	103.7	107.0
0.5	93.1	98.6	98.5	108.6	114.3	125.4	100.0	105.5	112.8
0.55	94.1	99.7	102.8	111.4	117.0	131.7	102.8	108.3	120.9
0.6	95.2	100.7	103.4	115.0	120.6	136.4	107.2	112.6	130.9
0.65	95.9	101.5	105.3	119.5	124.9	139.6	112.7	118.0	135.3
0.7	96.6	102.3	112.5	123.9	129.2	140.9	118.3	123.4	139.7
0.75	98.2	103.9	121.1	127.2	132.5	139.4	125.3	130.2	152.1
0.8	101.0	106.6	121.1	130.0	135.2	139.4	136.4	141.0	167.2
0.85	109.3	114.6	147.9	132.3	137.6	141.8	145.9	150.2	159.0
0.9	154.5	158.1	186.9	135.4	140.7	146.4	149.1	153.6	154.3
Average	95.0	100.3	107.4	110.0	115.6	125.5	107.4	112.6	121.0

80.8–149.1, 86.0–153.6, and 82.2–167.2 kJ/mol for the 1:1 BB-WT blend. The Friedman method shows higher E_α values compared to KAS and FWO for all the samples. This discrepancy, owing to the Friedman method, considers the differential form of the reaction rate, making it more sensitive to changes in the conversion rates and reaction kinetics. The agreement of our results with these known methodological characteristics further supports the robustness of the kinetic analysis, while the obtained E_α provides essential insights into the energy barriers associated with complex, multi-step degradation processes relevant to pyrolyzer design and optimization for efficient conversion processes[37].

As shown in Fig. 10, E_α for all three materials exhibited an upward trend with conversion, although with distinctly different growth rates. For BB (Fig. 10a), the E_a increases steadily as α rises from 0.1 to 0.8, followed by a sharp escalation at higher conversion. This behavior reflects the sequential decomposition of hemicellulose, cellulose, and finally lignin-rich aromatic structures, which require progressively higher energy barriers. In the case of WT (Fig. 10b), there was a consistent, nearly linear increase in E_α from 80 to 140 kJ/mol across the entire conversion range, consistent with the staged scission of natural rubber and styrene-butadiene rubber chains, sulfur crosslinks, and highly cross-linked aromatic residues. The behavior of the blend (Fig. 10c) shows two distinct regimes: below α = 0.4, E_α increases gradually, resembling the initial trend observed in BB, whereas above this threshold, the slope becomes significantly steeper, aligning with WT's characteristic progression. This indicates a transition from BB-dominated, to WT-influenced decomposition. As shown in Fig. 10d, the comparison of E_{Exp} and E_{Calc} provides preliminary indications of potential interactions during BB-WT co-pyrolysis. The experimental values represent the average E_α determined using the KAS, FWO, and Friedman methods, respectively. Across most of the conversion range, especially at high conversions (0.7–0.9), the E_{Exp} values of the blend were higher than that E_{Calc}, which may reflect inhibitory effects and complex multi-step reaction mechanisms during co-pyrolysis. Cross-linking occurs between sulfur-containing compounds from the WT, such as sulfides and vulcanized residues, and oxygen-rich fragments from the BB, particularly phenolic groups in lignin. This forms cross-linked structures, such as C-S-C bonds, which exhibit greater thermal stability, and consequently require higher energy for decomposition[27]. In contrast, within the conversion range of 0.3 to 0.5, E_{Calc} values exceed E_{Exp}, suggesting that a synergistic effect occurs due to radical stabilization and hydrogen transfer between BB-derived oxygenates and WT-derived hydrocarbons. As established by Kumar et al.[54], intense secondary reactions during co-pyrolysis form a dense, cross-linked char. This synergistically formed residue increases mass transfer resistance, requiring higher energy for volatile release and thereby elevating the experimental E_a.

Determination of the kinetic model function

The linear fitting results of $\ln(\frac{g(\alpha)}{T^2})$ vs $1/T$ for the pyrolysis of BB at different heating rates are summarized in Table 5. To identify the most suitable kinetic models, R2 values for each mechanism function across the four heating rates were examined. Higher R^2 values, closer to 1, indicate a better fit. D3, ZH, A1, A2/3, A1/2, A1/3, and A1/4 exhibited consistently high R^2 values at all heating rates. Among these, A2/3 stands out with an *E* of 105.61 kJ/mol, which is closest to the average *E* value of 100.91 kJ/mol determined by KAS, FWO and Friedman. This consistency indicates that the A2/3 mechanism function provides the best agreement for describing the pyrolysis of BB under the tested conditions.

As shown in Table 6, the mechanism functions, including F1, F3/2, D3, ZH, A1/2, A1/3, and A1/4, also show high R^2 values for WT. Notably, the F3/2 model yielded an *E* of 106.22 kJ/mol, which is close to the average value of 117.04 kJ/mol derived from the isoconversional methods. This suggests that the F3/2 mechanism is the most suitable for accurately describing the kinetics of WT pyrolysis.

As shown in Table 7, for the co-pyrolysis of BB and WT, several models, such as F1, F3/2, F2, D3, ZH, A1/3, and A1/4, achieved high R^2 values, with averages ranging from 0.984 to 0.996. The D3 mechanism function, with an average R^2 value of 0.984 and *E* of 116.49 kJ/mol, showed good agreement with the established *E* of 113.67 kJ/mol derived from the KAS, FWO, and Friedman methods. Thus, D3 is considered the most appropriate model for representing the co-pyrolysis kinetics of the BB-WT blend.

The kinetic analysis revealed a distinct mechanistic shift: BB followed random nucleation and subsequent growth (A2/3), WT followed a chemical reaction (F3/2), while their blend followed three-dimensional diffusion (D3). This shift provides direct evidence

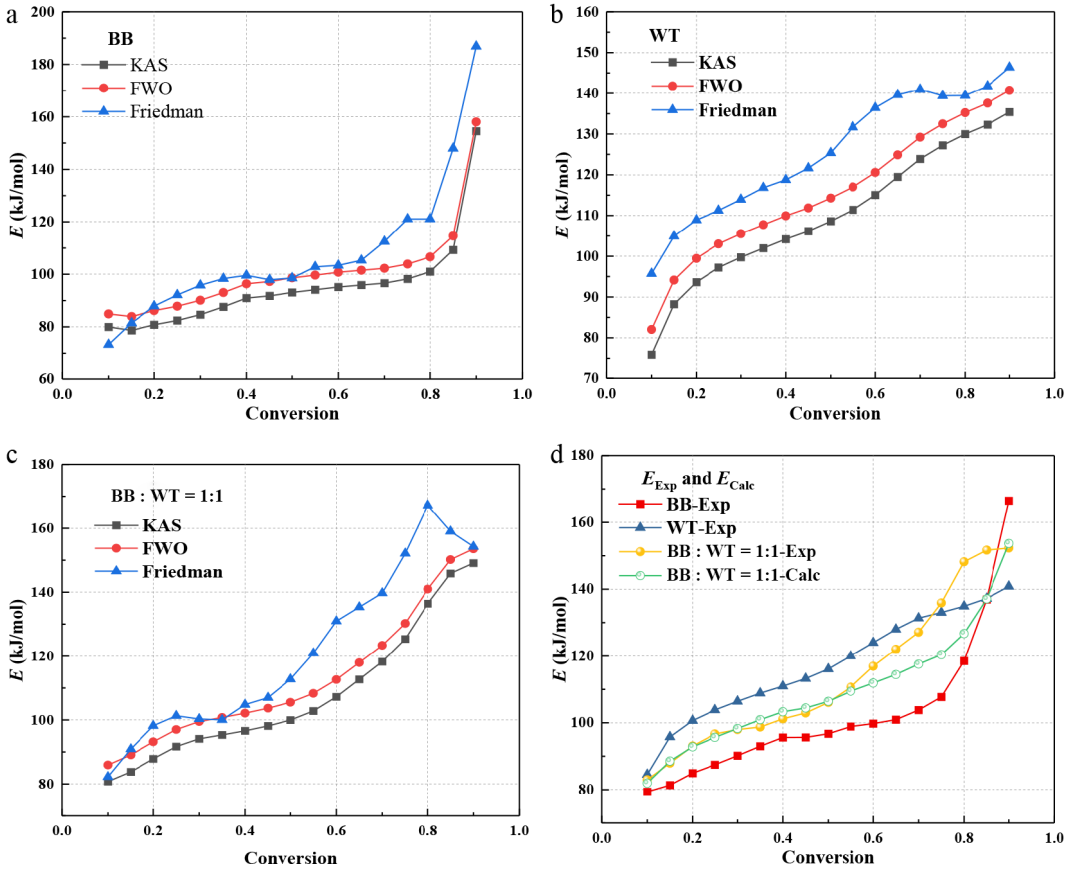

Fig. 10 E_α of BB, WT and the 1:1 BB-WT blend.

Table 5. The R^2 of linear fitting of $\ln(\frac{g(\alpha)}{T^2})$ vs $1/T$ for BB.

No.	Code	10 °C/min		20 °C/min		30 °C/min		40 °C/min		Average R^2	Average E
		R^2	E	R^2	E	R^2	E	R^2	E		
1	F1	0.982	61.24	0.987	66.01	0.991	69.58	0.992	70.85	0.988	66.92
2	F3/2	0.984	74.27	0.985	79.96	0.985	84.18	0.983	85.41	0.984	80.96
3	F2	0.975	89.23	0.974	95.95	0.969	100.92	0.965	102.08	0.971	97.05
4	F3	0.945	123.89	0.940	133.02	0.931	139.70	0.922	140.67	0.935	134.32
5	D1	0.950	92.37	0.958	99.37	0.970	104.62	0.977	107.33	0.964	100.92
6	D2	0.965	103.44	0.972	111.23	0.982	117.07	0.987	119.81	0.977	112.89
7	**D3**	**0.980**	**117.47**	**0.984**	**126.26**	**0.990**	**132.83**	**0.993**	**135.56**	**0.987**	**128.03**
8	G-B	0.970	108.05	0.977	116.18	0.985	122.26	0.990	124.99	0.981	117.87
9	**ZH**	**0.987**	**149.54**	**0.989**	**160.59**	**0.989**	**168.79**	**0.988**	**171.44**	**0.988**	**162.59**
10	R1	0.935	41.12	0.947	44.46	0.962	46.98	0.971	48.25	0.954	45.20
11	R2	0.967	50.22	0.974	54.21	0.984	57.21	0.989	58.50	0.979	55.04
12	R3	0.973	53.67	0.980	57.91	0.988	61.09	0.992	62.37	0.983	58.76
13	A3/2	0.979	37.45	0.984	40.52	0.989	42.83	0.991	43.63	0.986	41.11
14	A2	0.974	25.56	0.981	27.78	0.987	29.46	0.989	30.02	0.983	28.21
15	A3	0.958	13.66	0.970	15.04	0.981	16.09	0.985	16.40	0.974	15.30
16	A4	0.924	7.71	0.948	8.67	0.969	9.40	0.976	9.60	0.954	8.85
17	**A1**	**0.982**	**61.24**	**0.987**	**66.01**	**0.991**	**69.58**	**0.992**	**70.85**	**0.988**	**66.92**
18	**A2/3**	**0.984**	**96.92**	**0.988**	**104.24**	**0.992**	**109.69**	**0.993**	**111.60**	**0.989**	**105.61**
19	**A1/2**	**0.985**	**132.61**	**0.989**	**142.47**	**0.992**	**149.81**	**0.993**	**152.51**	**0.990**	**144.35**
20	**A1/3**	**0.986**	**203.96**	**0.989**	**218.93**	**0.993**	**230.04**	**0.993**	**234.18**	**0.990**	**221.78**
21	**A1/4**	**0.986**	**275.34**	**0.990**	**295.39**	**0.993**	**310.27**	**0.994**	**315.85**	**0.991**	**299.21**
22	P1	0.430	2.68	0.550	3.28	0.676	3.76	0.738	3.95	0.599	3.42
23	P2	0.763	6.95	0.813	7.85	0.869	8.56	0.897	8.87	0.836	8.06
24	P3	0.882	15.50	0.907	17.01	0.934	18.16	0.975	18.72	0.925	17.35

Values in boldface indicate the reaction mechanism models with better fitting results.

of synergistic interactions, where cross-linking reactions between the feedstocks form a denser char residue, thereby altering the rate-limiting step to mass transport of volatiles[55]. The prolonged residence time of volatile components within the dense coke matrix promotes secondary reactions, such as the hydrogenation-deoxygenation of phenolic compounds by WT-derived hydrogen, and the stabilisation of olefinic fragments. These processes collectively account for the significant reduction in oxygen-containing compounds identified by GC/MS, and the enrichment of hydrocarbons.

Table 6. The R^2 of linear fitting of $\ln(\frac{g(\alpha)}{T^2})$ vs $1/T$ for WT.

No.	Code	10 °C/min		20 °C/min		30 °C/min		40 °C/min		Average R^2	Average *E*
		R^2	*E*	R^2	*E*	R^2	*E*	R^2	*E*		
1	F1	0.986	78.64	0.986	85.50	0.985	85.50	0.987	97.78	0.986	86.86
2	**F3/2**	**0.986**	**95.03**	**0.987**	**103.35**	**0.986**	**108.45**	**0.991**	**118.03**	**0.988**	**106.22**
3	F2	0.977	113.82	0.979	123.83	0.977	130.02	0.985	141.27	0.980	127.24
4	F3	0.946	157.38	0.949	171.31	0.948	180.04	0.958	195.18	0.950	175.98
5	D1	0.953	117.76	0.951	127.43	0.952	133.13	0.947	145.08	0.951	130.85
6	D2	0.968	131.71	0.967	142.58	0.967	149.05	0.964	162.25	0.967	146.40
7	D3	0.981	149.38	0.981	161.80	0.980	169.27	0.980	184.04	0.981	166.12
8	G-B	0.973	137.53	0.972	148.90	0.972	155.70	0.970	169.41	0.972	152.89
9	**ZH**	**0.989**	**189.73**	**0.989**	**205.71**	**0.988**	**215.49**	**0.992**	**233.85**	**0.990**	**211.20**
10	R1	0.942	53.30	0.940	57.96	0.942	60.69	0.937	66.55	0.940	59.63
11	R2	0.971	64.77	0.971	70.42	0.971	73.79	0.969	80.67	0.971	72.41
12	R3	0.978	69.12	0.977	75.14	0.977	78.76	0.977	86.03	0.977	77.26
13	A3/2	0.983	48.71	0.984	53.16	0.983	55.86	0.985	61.20	0.984	54.73
14	A2	0.980	33.74	0.981	36.99	0.980	38.96	0.983	42.90	0.981	38.15
15	A3	0.972	18.78	0.973	20.82	0.973	22.05	0.976	24.61	0.974	21.57
16	A4	0.956	11.29	0.960	12.74	0.959	13.60	0.966	15.46	0.960	13.27
17	A1	0.986	78.64	0.986	85.50	0.985	89.66	0.987	97.78	0.986	87.90
18	A2/3	0.987	123.54	0.987	134.01	0.986	140.37	0.988	152.66	0.987	137.65
19	**A1/2**	**0.987**	**168.43**	**0.988**	**182.53**	**0.987**	**191.08**	**0.989**	**207.54**	**0.988**	**187.40**
20	**A1/3**	**0.988**	**258.22**	**0.988**	**279.55**	**0.987**	**292.49**	**0.989**	**317.30**	**0.988**	**286.89**
21	**A1/4**	**0.988**	**348.02**	**0.988**	**376.57**	**0.988**	**393.91**	**0.989**	**427.07**	**0.988**	**386.39**
22	P1	0.658	4.96	0.692	5.85	0.714	6.36	0.736	7.65	0.700	6.21
23	P2	0.833	10.33	0.841	11.64	0.849	12.40	0.849	14.20	0.843	12.14
24	P3	0.906	21.08	0.907	23.22	0.910	24.47	0.905	27.29	0.907	24.02

Values in boldface indicate the reaction mechanism models with better fitting results.

Table 7. The R^2 of linear fitting of $\ln(\frac{g(\alpha)}{T^2})$ vs $1/T$ for the 1:1 BB-WT blend.

No.	Code	10 °C/min		20 °C/min		30 °C/min		40 °C/min		Average R^2	Average *E*
		R^2	*E*	R^2	*E*	R^2	*E*	R^2	*E*		
1	**F1**	**0.987**	**53.13**	**0.99**	**58.42**	**0.993**	**63.88**	**0.995**	**65.6**	**0.991**	**60.26**
2	**F3/2**	**0.996**	**64.99**	**0.997**	**71.29**	**0.994**	**77.97**	**0.995**	**79.64**	**0.996**	**73.47**
3	**F2**	**0.993**	**78.6**	**0.991**	**86.08**	**0.984**	**94.14**	**0.985**	**95.75**	**0.988**	**88.64**
4	F3	0.97	110.18	0.965	120.37	0.951	131.65	0.952	133.09	0.960	123.82
5	D1	0.936	80.35	0.945	88.06	0.957	96.68	0.959	99.09	0.949	91.05
6	D2	0.957	90.39	0.964	98.96	0.974	108.65	0.975	111.04	0.968	102.26
7	**D3**	**0.977**	**103.14**	**0.982**	**112.81**	**0.988**	**123.82**	**0.989**	**126.18**	**0.984**	**116.49**
8	G-B	0.967	94.58	0.971	103.52	0.98	113.64	0.981	116.02	0.975	106.94
9	**ZH**	**0.996**	**132.3**	**0.997**	**144.48**	**0.996**	**158.51**	**0.997**	**160.75**	**0.997**	**149.01**
10	R1	0.913	34.86	0.926	38.57	0.94	42.12	0.947	43.9	0.932	39.86
11	R2	0.959	43.12	0.968	47.54	0.976	51.96	0.979	53.72	0.971	49.09
12	R3	0.971	46.26	0.977	50.94	0.984	55.69	0.986	57.44	0.980	52.58
13	A3/2	0.983	31.88	0.988	35.3	0.991	38.44	0.993	39.97	0.989	36.40
14	A2	0.977	21.25	0.984	23.75	0.987	25.72	0.992	27.15	0.985	24.47
15	A3	0.955	10.63	0.97	12.19	0.973	13	0.985	14.33	0.971	12.54
16	A4	0.894	5.31	0.935	6.41	0.932	6.64	0.971	7.93	0.933	6.57
17	A1	0.987	53.13	0.99	58.42	0.993	63.88	0.995	65.6	0.991	60.26
18	A2/3	0.989	85.01	0.992	93.09	0.994	102.06	0.995	104.05	0.993	96.05
19	**A1/2**	**0.99**	**116.89**	**0.992**	**127.75**	**0.995**	**140.19**	**0.996**	**142.5**	**0.993**	**131.83**
20	**A1/3**	**0.99**	**180.65**	**0.993**	**197.09**	**0.995**	**216.51**	**0.996**	**219.4**	**0.994**	**203.41**
21	**A1/4**	**0.991**	**244.41**	**0.993**	**266.43**	**0.995**	**292.82**	**0.996**	**296.29**	**0.994**	**274.99**
22	P1	0.062	0.75	0.143	1.45	0.065	1.2	0.405	2.5	0.169	1.48
23	P2	0.568	4.54	0.665	5.58	0.654	5.75	0.78	7.1	0.667	5.74
24	P3	0.823	12.12	0.856	13.82	0.869	14.84	0.9	16.3	0.862	14.27

Values in boldface indicate the reaction mechanism models with better fitting results.

Kinetic compensation effect

Figure 11 illustrates the linear regression results for the different samples in the KCE analysis. Figure 11a presents the regression analysis for the BB, with a regression equation of $\ln(A_\alpha) = 0.129E_\alpha + 3.485$, with R^2 = 0.965, indicating a robust linear relationship. In Fig. 11b, WT exhibits a regression equation of $\ln(A_\alpha) = 0.168E_\alpha - 2.461$, and R^2 = 0.993, demonstrating an excellent fit. Figure 11c shows the 1:1 blend of BB and WT, with the regression equation $\ln(A_\alpha) = 0.175E_\alpha - 5.038$, and R^2 = 0.985.

These regression plots confirm the presence of the KCE, a well-established phenomenon in thermal kinetics, which manifests as a linear correlation between E_α and $\ln(A_\alpha)$. In this work, the KCE analysis is employed as a consistency and reliability check of the kinetic parameters derived from the isoconversional methods. This provides both internal validation of the obtained parameters, and confidence in their reliability when comparing different feedstocks and their blend. The high coefficients of determination ($R^2 > 0.96$) obtained for BB, WT, and their blends further indicate that the extracted kinetic parameters are internally consistent and thus suitable for predictive modeling of the thermal behavior.

Conclusions

This study comprehensively evaluated the co-pyrolysis behavior and kinetic characteristics of BB, WT, and their blends. The main conclusions are summarized as follows:

(1) BB and WT exhibit different thermal degradation characteristics, and co-pyrolysis significantly alters the thermal stability and decomposition behavior. The presence of WT in the blend enhances overall thermal stability and reduces weight loss, making the pyrolysis process more gradual and stable, which is advantageous for process control and operational stability in continuous reactors.

(2) The chemical composition of the pyrolysis products is strongly influenced by the BB-WT ratio. Proper blending ratios can effectively suppress oxygenated compounds (such as phenolics and ketones), while maintaining a high proportion of hydrocarbons, thereby improving fuel quality and enhancing the potential for valuable chemical production. This provides a practical strategy for optimizing energy recovery and chemical production in waste-to-energy systems.

(3) The average values of E_α for BB, WT, and their 1:1 blend are 101.91, 117.04, and 113.67 kJ/mol, respectively. The A2/3, F3/2, and D3 models are identified as the most suitable mechanisms for BB, WT, and their 1:1 blend. The linear relationship($R^2 > 0.965$) between the E_α and the $\ln(A_\alpha)$ confirms the reliability of the kinetic parameters, which are essential for predictive modeling of large-scale operations.

(4) The ΔW and Δr, FTIR analysis, and GC/MS analysis suggest that synergistic effects occur between 300–500 °C, particularly for BB : WT = 5:5 and 3:7. The hydrogen-rich fragments from WT promote the deoxygenation of BB-derived intermediates, reducing phenolics, while oxygen radicals from BB enhance WT chain scission, increasing aromatics and alkenes. These interactions reveal optimal blending strategies for improving co-pyrolysis efficiency and product quality.

Overall, this study provides crucial insights into the design, modeling, and optimization of waste-to-energy pyrolysis systems

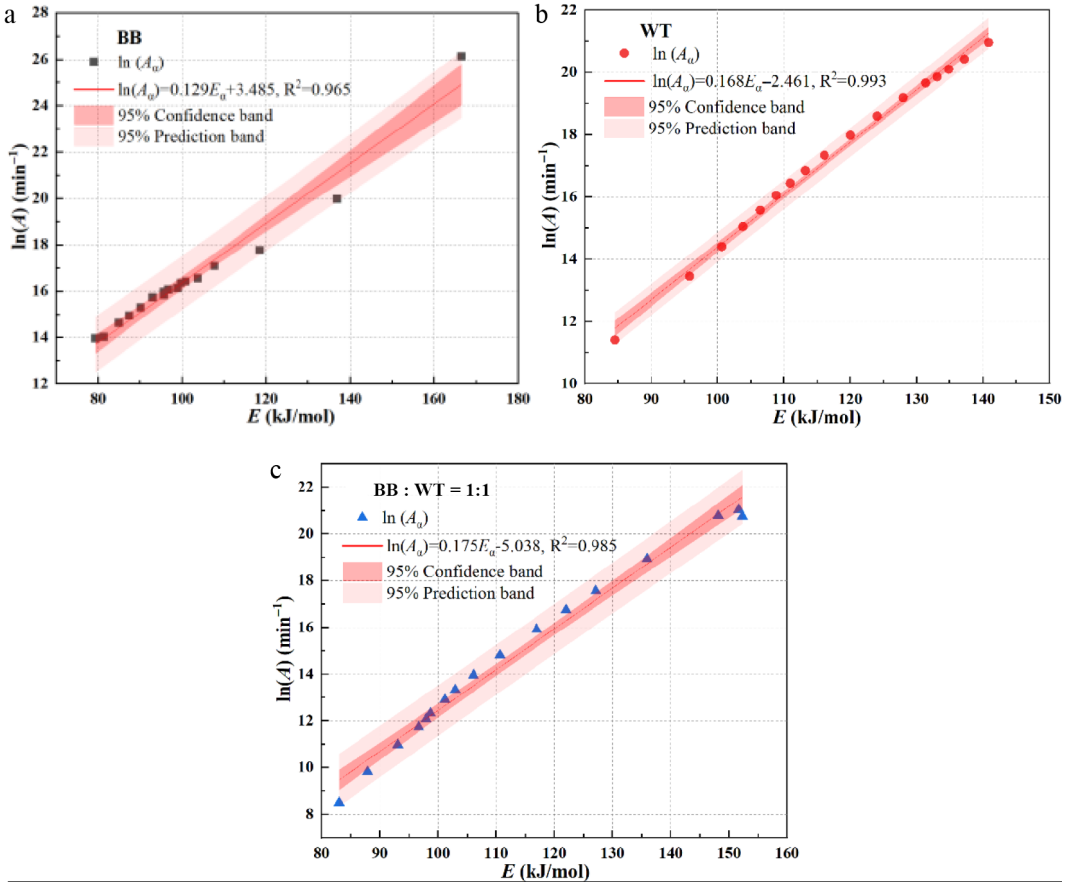

Fig. 11 Linear regression of the compensation effect.

handling mixed biomass and polymeric wastes. This work defines optimal co-pyrolysis parameters for industrial application: using a 3:7 or 5:5 bamboo-to-tire blend within a 300–500 °C window maximizes hydrocarbon production by exploiting synergistic radical interactions. The provided kinetic data and reaction model enable direct scaling for efficient bio-oil production from waste.

However, as a lab-scale study, limitations exist regarding heat/mass transfer effects and continuous operation for industrial application. Future work should therefore focus on: (1) Pilot-scale validation to verify the synergies and kinetic models in continuous-fed reactors; (2) Comprehensive char characterization to understand the impact of interactions on biochar yield, surface properties, and stability[31]; (3) Catalytic upgrading of the synergistic, hydrocarbon-rich bio-oil to produce high-value fuels or chemicals.

Author contributions

The authors confirm their contributions to the paper as follows: investigation, methodology, data curation, original draft preparation: Bai Y; conceptualization, formal analysis, visualization, writing review and editing, funding acquisition: Du N; investigation, data curation, validation: Zhou Z; resources, supervision, writing review and editing, project administration, funding acquisition: Ma H. All authors reviewed the results and approved the final version of the manuscript.

Data availability

The datasets generated during and/or analyzed in the current study are available from the corresponding author on reasonable request.

Acknowledgments

This work was supported by the China National Key R&D Program (Grant No. 2022YFC3902302), the Natural Science Foundation of Hebei Province (Grant No. E2023203166), and Department of Education of Hebei Province (QN2025058).

Conflict of interest

The authors declare that they have no known competing financial interests or personal relationships that could have appeared to influence the work reported in this paper.

Supplementary information accompanies this paper online at: https://doi.org/10.48130/prkm-0026-0002.

Dates

Received 26 June 2025; Revised 12 November 2025; Accepted 14 January 2026; Published online 9 May 2026

References

[1] Aniza R, Chen WH, Lin YY, Tran KQ, Chang JS, et al. 2021. Independent parallel pyrolysis kinetics of extracted proteins and lipids as well as model carbohydrates in microalgae. *Applied Energy* 300:117372

[2] Aboelela D, Saleh H, Attia AM, Elhenawy Y, Majozi T, et al. 2023. Recent advances in biomass pyrolysis processes for bioenergy production: optimization of operating conditions. *Sustainability* 15:11238

[3] Yuen JQ, Fung T, Ziegler AD. 2017. Carbon stocks in bamboo ecosystems worldwide: Estimates and uncertainties. *Forest Ecology and Management* 393:113–138

[4] Bahari SA, Krause A. 2016. Utilizing Malaysian bamboo for use in thermoplastic composites. *Journal of Cleaner Production* 110:16–24

[5] Li C, Li L, Yellezuome D, Cai J, Liu R, et al. 2023. Physicochemical investigation and thermogravimetric analysis of bamboo and poplar wood residues and tire rubber waste: kinetic and thermodynamic analyses. *Industrial Crops and Products* 206:117715

[6] Abioye KJ, Falua KJ, Rezaee M, Zamiri MA, Zou F, et al. 2025. Global insights into biomass pyrolysis mechanisms: a scientometric and mechanistic approach. *Results in Engineering* 28:107123

[7] Lin Y, Ye R, Lu Z, Ge Y, Xiao H, et al. 2025. Ca-catalyzed co-pyrolysis behavior of biomass and waste plastics: a ReaxFF molecular dynamics simulation and experiments study. *Journal of the Energy Institute* 122:102225

[8] Shan Ahamed T, Anto S, Mathimani T, Brindhadevi K, Pugazhendhi A. 2021. Upgrading of bio-oil from thermochemical conversion of various biomass – mechanism, challenges and opportunities. *Fuel* 287:119329

[9] Singh M, Salaudeen SA, Gilroyed BH, Al-Salem SM, Dutta A. 2023. A review on co-pyrolysis of biomass with plastics and tires: recent progress, catalyst development, and scaling up potential. *Biomass Conversion and Biorefinery* 13:8747–8771

[10] Liu P, Jiang Z, Zeng Y, Wang Y, Zeng C, et al. 2024. Microwave-enhanced pyrolysis of bamboo for furfural-rich bio-oil production over WS_2 catalyst. *Industrial Crops and Products* 216:118768

[11] Jiang H, Shao JA, Zhu Y, Yu J, Cheng W, et al. 2023. Production mechanism of high-quality carbon black from high-temperature pyrolysis of waste tire. *Journal of Hazardous Materials* 443:130350

[12] Gao N, Wang F, Quan C, Santamaria L, Lopez G, et al. 2022. Tire pyrolysis char: processes, properties, upgrading and applications. *Progress in Energy and Combustion Science* 93:101022

[13] Zhang G, Chen F, Zhang Y, Zhao L, Chen J, et al. 2021. Properties and utilization of waste tire pyrolysis oil: a mini review. *Fuel Processing Technology* 211:106582

[14] Czarna-Juszkiewicz D, Kunecki P, Cader J, Wdowin M. 2023. Review in waste tire management – potential applications in mitigating environmental pollution. *Materials* 16:5771

[15] Kandasamy J, Gökalp I. 2015. Pyrolysis, combustion, and steam gasification of various types of scrap tires for energy recovery. *Energy & Fuels* 29:346–354

[16] Lewandowski WM, Januszewicz K, Kosakowski W. 2019. Efficiency and proportions of waste tyre pyrolysis products depending on the reactor type – a review. *Journal of Analytical and Applied Pyrolysis* 140:25–53

[17] Uyumaz A, Aydoğan B, Solmaz H, Yılmaz E, Yeşim Hopa D, et al. 2019. Production of waste tyre oil and experimental investigation on combustion, engine performance and exhaust emissions. *Journal of the Energy Institute* 92:1406–1418

[18] Narani SS, Abbaspour M, Mir Mohammad Hosseini SM, Aflaki E, Nejad FM. 2020. Sustainable reuse of waste tire textile fibers (WTTFs) as reinforcement materials for expansive soils: with a special focus on landfill liners/covers. *Journal of Cleaner Production* 247:119151

[19] Niu M, Sun R, Ding K, Gu H, Cui X, et al. 2022. Synergistic effect on thermal behavior and product characteristics during co-pyrolysis of biomass and waste tire: influence of biomass species and waste blending ratios. *Energy* 240:122808

[20] Ramarad S, Khalid M, Ratnam CT, Chuah AL, Rashmi W. 2015. Waste tire rubber in polymer blends: a review on the evolution, properties and future. *Progress in Materials Science* 72:100–140

[21] Hassan H, Lim JK, Hameed BH. 2016. Recent progress on biomass co-pyrolysis conversion into high-quality bio-oil. *Bioresource Technology* 221:645–655

[22] Wang J, Zhong Z, Ding K, Zhang B, Deng A, et al. 2017. Co-pyrolysis of bamboo residual with waste tire over dual catalytic stage of CaO and co-modified HZSM-5. *Energy* 133:90–98

[23] Wang L, Chai M, Liu R, Cai J. 2018. Synergetic effects during co-pyrolysis of biomass and waste tire: a study on product distribution and reaction kinetics. *Bioresource Technology* 268:363–370

[24] Azizi K, Moshfegh Haghighi A, Keshavarz Moraveji M, Olazar M, Lopez G. 2019. Co-pyrolysis of binary and ternary mixtures of microalgae, wood and waste tires through TGA. *Renewable Energy* 142:264–271
[25] Kumar A, Yan B, Tao J, Li J, Kumari L, et al. 2022. Co-pyrolysis of de-oiled microalgal biomass residue and waste tires: deeper insights from thermal kinetics, behaviors, drivers, bio-oils, bio-chars, and in-situ evolved gases analyses. *Chemical Engineering Journal* 446:137160
[26] Farooq MZ, Zeeshan M, Iqbal S, Ahmed N, Shah SAY. 2018. Influence of waste tire addition on wheat straw pyrolysis yield and oil quality. *Energy* 144:200–206
[27] Guo Q, Zhang Z, Zhao L, Wang X, Hu Y. 2023. Release and evolution mechanism of oxygen-containing compounds and aromatics during the co-pyrolysis of waste tire and bamboo sawdust/rice husk by Py-GC/MS. *Journal of Analytical and Applied Pyrolysis* 170:105923
[28] Wang J, Zhong Z, Ding K, Li M, Hao N, et al. 2019. Catalytic fast co-pyrolysis of bamboo sawdust and waste tire using a tandem reactor with cascade bubbling fluidized bed and fixed bed system. *Energy Conversion and Management* 180:60–71
[29] Wang Y, Dai L, Fan L, Duan D, Liu Y, et al. 2017. Microwave-assisted catalytic fast co-pyrolysis of bamboo sawdust and waste tire for bio-oil production. *Journal of Analytical and Applied Pyrolysis* 123:224–228
[30] Deng N, Ye Y, Yao X, Ren Z, Zhang Q, et al. 2025. Synergistic co-pyrolysis characteristics of waste tire and moso bamboo: mechanisms and kinetics. *Chemical Engineering Journal* 525:170225
[31] Kumar A, Kumari L, Ali Laghari A, Rong H, Ali Jamro I, et al. 2024. Exploring the integrated potential of pyrolysis and low-temperature wet torrefaction for typical medical waste valorization: a multifaceted approach leveraging online TG-FTIR-MS, 2D-COS, *iso*-conversional kinetics, and reaction mechanisms. *Chemical Engineering Journal* 499:156464
[32] Garcia-Maraver A, Perez-Jimenez JA, Serrano-Bernardo F, Zamorano M. 2015. Determination and comparison of combustion kinetics parameters of agricultural biomass from olive trees. *Renewable Energy* 83:897–904
[33] Diblasi C. 2008. Modeling chemical and physical processes of wood and biomass pyrolysis. *Progress in Energy and Combustion Science* 34:47–90
[34] GB/T 28731-2012: *Proximate Analysis of Solid Biofuels*. Standardization Administration of the People's Republic of China. https://openstd.samr.gov.cn/bzgk/gb/newGbInfo?hcno=E2D830152F09E47F4F6F7FF84555C30B
[35] CJ/T 313-2009: *Sampling and analysis methods for domestic waste*. Standardization Administration of the People's Republic of China. https://std.samr.gov.cn/hb/search/stdHBDetailed?id=8B1827F1BFD7BB19E05397BE0A0AB44A
[36] CJ/T 96-2013: *General detecting methods for the chemical characteristics of domestic refuse*. Standardization Administration of the People's Republic of China. https://std.samr.gov.cn/hb/search/stdHBDetailed?id=8B1827F19576BB19E05397BE0A0AB44A
[37] Mishra RK, Chinnam S, Mohanty K. 2025. Kinetic behaviour and fast pyrolysis of *Tamarindus indica* seeds using Py-GC–MS. *Bioresource Technology Reports* 29:102014
[38] Kissinger HE. 1957. Reaction kinetics in differential thermal analysis. *Analytical Chemistry* 29:1702–1706
[39] Akahira T, Sunose T. 1971. Method of determining activation deterioration constant of electrical insulating materials. *Research Reports of Chiba Institute of Technology (Science and Technology)* 16:22–31
[40] Flynn JH, Wall LA. 1966. A quick, direct method for the determination of activation energy from thermogravimetric data. *Journal of Polymer Science Part B: Polymer Letters* 4:323–328
[41] Ozawa T. 1965. A New method of analyzing thermogravimetric data. *Bulletin of the Chemical Society of Japan* 38:1881–1886
[42] Friedman HL. 1964. Kinetics of thermal degradation of char-forming plastics from thermogravimetry. Application to a phenolic plastic. *Journal of Polymer Science Part C: Polymer Symposia* 6:183–195
[43] Mishra RK, Chinnam S, Sharma A. 2024. Catalytic co-pyrolysis behaviour and kinetics study of waste lignocellulosic non-edible seeds and Covid-19 plastic over Al_2O_3 catalyst. *Bioresource Technology Reports* 27:101899
[44] Heydari M, Rahman M, Gupta R. 2015. Kinetic study and thermal decomposition behavior of lignite coal. *International Journal of Chemical Engineering* 2015:481739
[45] Criado JM, Ortega A. 1985. The accuracy of equation approximating the integral of the Arrhenius equation to perform the kinetic analysis of solid state reactions. *International Journal of Chemical Kinetics* 17:1365–1373
[46] Coats AW, Redfern JP. 1964. Kinetic parameters from thermogravimetric data. *Nature* 201:68–69
[47] Söyler N, Ceylan S. 2021. Thermokinetic analysis and product characterization of waste tire-hazelnut shell co-pyrolysis: TG-FTIR and fixed bed reactor study. *Journal of Environmental Chemical Engineering* 9:106165
[48] Kumar A, Ali Jamro I, Rong H, Kumari L, Ali Laghari A, et al. 2024. Assessing bioenergy prospects of algal biomass and yard waste using an integrated hydrothermal carbonization and pyrolysis (HTC–PY): a detailed emission–to–ash characterization via diverse hyphenated analytical techniques and modelling strategies. *Chemical Engineering Journal* 492:152335
[49] Chen H, Wang J, Rocha LA, Zhang H, Zhang S, et al. 2024. Insights into the char-production mechanism during co-pyrolysis of biomass and plastic wastes. *Energy* 312:133642
[50] Weng S. 2010. *Fourier Transform Infrared Spectroscopy Analysis*. Beijing: Chemical Industry Press. https://search.worldcat.org/title/862660505
[51] Pinto O, Romero R, Carrier M, Appelt J, Segura C. 2018. Fast pyrolysis of tannins from pine bark as a renewable source of catechols. *Journal of Analytical and Applied Pyrolysis* 136:69–76
[52] Xu F, Wang B, Yang D, Hao J, Qiao Y, et al. 2018. Thermal degradation of typical plastics under high heating rate conditions by TG-FTIR: pyrolysis behaviors and kinetic analysis. *Energy Conversion and Management* 171:1106–1115
[53] Park KB, Kim JS. 2023. Pyrolysis products from various types of plastics using TG-FTIR at different reaction temperatures. *Journal of Analytical and Applied Pyrolysis* 171:105983
[54] Kumar A, Ali Jamro I, Wang J, Ullah A, Kumari L, et al. 2024. Co-pyrolysis of microalgae residue and sewage sludge: an in-depth characterization of kinetics, drivers, and gas-oil-char behaviors. *Journal of Analytical and Applied Pyrolysis* 179:106438
[55] Kumar A, Ali Jamro I, Yan B, Cheng Z, Tao J, et al. 2023. Pyrolysis of defatted microalgae residue: a study on thermal-kinetics, products' optimization, and neural network modelling. *Fuel* 334:126752